Copyright WILEY-VCH Verlag GmbH & Co. KGaA, 69469 Weinheim, Germany, 2013.

# Supporting Information

## Chemically Selective Alternatives to Photoferroelectrics for Polarization-Enhanced Photocatalysis: the Untapped Potential of Hybrid Inorganic Nanotubes

*Joshua D. Elliott, Emiliano Poli, Ivan Scivetti, Laura E. Ratcliff, Lampros Andrinopoulos, Jacek Dziedzic, Nicholas D. M. Hine, Arash A. Mostofi, Chris-Kriton Skylaris, Peter D. Haynes, Gilberto Teobaldi**

### 1. Supplementary methods

#### Potential step in a co-axial cylindrical capacitor

As shown in Figure 3a, in spite of the NT-wall polarization, and owing to the NT cylindrical symmetry and overall charge-neutrality, the NTs present a flat electrostatic potential [$V(\mathbf{r})$] inside and outside the NT-cavity. Since the electrostatic field ($\vec{\mathbf{E}}$) is given by the negative gradient of the electrostatic potential [$\vec{\mathbf{E}} = -\nabla V(\mathbf{r})$], no electrostatic field is present inside and outside the NT. As a result, it is possible to model the NT electrostatics on the basis of an overall neutral co-axial (hollow) cylindrical capacitor (Figure S1).

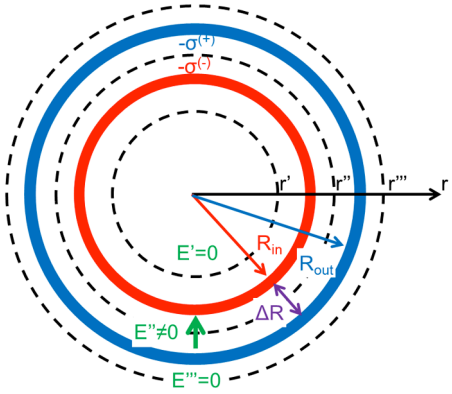



**Figure S1.** Front view of a cylindrical co-axial capacitor with charge $-Q = -\sigma^{(-)} 2\pi R_{in} L$ and $Q = \sigma^{(+)} 2\pi R_{out} L$ on the inner and outer hollow cylinder, respectively. $L$ is the length of the inner and outer hollow cylinders. The three cylindrical Gaussian surfaces of radius $r'$, $r''$, and $r'''$ are also indicated.

Gauss' theorem relates the flux of the electrostatic field ($\vec{\mathbf{E}}$) across a closed surface ($S$) to the charge $Q$ contained inside the closed surface:

$$\frac{Q}{\varepsilon_0} = \oint_S \vec{\mathbf{E}} \cdot \mathbf{d\hat{s}} \tag{S1}$$

where $\varepsilon_0$ is the electric permittivity of vacuum, and $\mathbf{d\hat{s}}$ a vector of unitary module locally normal to the infinitesimal surface element. Eq. S1 allows definition of three electrostatic regions with different in the co-axial capacitor in Figure S1:

**Region 1.** For $r < R_{in}$, the electric field is zero ($E = 0$) since the Gaussian surface of radius $r'$ does not contain any net charge ($Q = 0$).

**Region 2.** For $R_{in} \leq r < R_{out}$, the electric field is not zero ($E \neq 0$) since the Gaussian surface of radius $r''$ does contain a net charge ($-Q < 0$, see Figure S1). As the hollow cylinders are taken to be in electrostatic equilibrium, with no net transfer of charge, $\mathbf{E} = E\hat{\mathbf{r}}$ i.e. the electrostatic field must lie parallel to the tube radius, with zero components along the tube (lateral) surface.

**Region 3.** For $r > R_{out}$, the electric field is zero ($E = 0$) since the Gaussian surface of radius $r'''$ does not contain any net charge ($Q = 0$), being the cylindrical capacitor overall neutral.

We thus focus in Region 2 to calculate the electric field and potential difference between $R_{in}$ and $R_{out}$ by Gauss' flux theorem. We start by expanding both sides of Eq. S1 as:

$$\frac{Q}{\varepsilon_0} = \frac{-2\pi R_{in} L \sigma^{(-)}}{\varepsilon_0} = \oint_S \vec{\mathbf{E}} \cdot \mathbf{d\hat{s}} = 2\pi r'' LE \tag{S2}$$

Where in the right-side term we have taken advantage of $\vec{\mathbf{E}}$ being locally parallel to $\mathbf{d\hat{s}}$ and that the $\vec{\mathbf{E}}$ between the cylinders has to be directed parallel to the surface normal with zero components along the cylinder axis.

Eq. S2 can be rearranged to read:

$$\frac{-R_{in}\sigma^{(-)}}{\varepsilon_0 r''} = E = -\frac{dV}{dr''} \tag{S3}$$

which allows the integration of the electrostatic potential between $R_{in}$ and $R_{out}$ as:

$$\Delta V = V(R_{in}) - V(R_{out}) = \int_{R_{out}}^{R_{in}} dr'' E = \frac{R_{in}\sigma^{(-)}}{\varepsilon_0} \int_{R_{out}}^{R_{in}} dr'' \frac{1}{r''} = \frac{R_{in}\sigma^{(-)}}{\varepsilon_0} \ln\left(\frac{R_{in}}{R_{out}}\right) \tag{S4}$$

It is worth noting that, in Eq. S4, the overall negative sign of $\Delta V = V(R_{in}) - V(R_{out})$ [$\ln\left(R_{in}/R_{out}\right) < 0$] is consistent with $\vec{\mathbf{E}}$ being directed from the outer (positively charged) to the inner (negatively charged) cylinder (Figure S1).

In analogy with the treatment for the surface dipole density ( $\mu_\sigma$) due to two charged surfaces (of surface charge-density $\sigma$) locally parallel and separated by a distance *d*:[S1]

$$\lim_{d\to 0} \sigma d = \mu_\sigma \tag{S5}$$

For infinitesimally small separation $\Delta R$, leading to $R_{in} = R_{out}$ and $\sigma^{(-)} = \sigma^{(+)} = \sigma$, the separation in surface charge density ($\sigma$) between the inner and outer cylinders (Figure S2) can be described via a surface dipole-density as:

$$\lim_{\Delta R\to 0} \sigma \Delta R = \mu_\sigma \tag{S6}$$

which in turn can be used to write:

$$\sigma = \frac{\mu_\sigma}{\Delta R} \tag{S7}$$

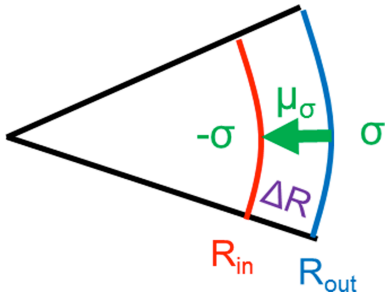



**Figure S2.** Separation of charge density ($\sigma$) between the co-axial cylinders, leading to a surface dipole-density $\mu_\sigma$.

Although Eq. S5 is strictly verified for infinitesimally small separations between the charge-layers (*d*), it is routinely used in the modelling of potential steps across atomically heterogeneous bi-dimensional junctions (of finite thickness) between different materials (see, for instance, Ref. [S2] and references therein). Therefore, by using Eq. S6, we resort to the same approximation in computing the potential step across the interface dipole at the NT-wall of atomically finite thickness $\Delta R \neq 0$. Accordingly, and based on Eq. S7, Eq. S4 can be rearranged into:

$$\Delta V = V(R_{in}) - V(R_{out}) = \frac{R_{in}\sigma}{\varepsilon_0} \ln\left(\frac{R_{in}}{R_{out}}\right) = \frac{R_{in}}{\varepsilon_0}\frac{\mu_\sigma}{\Delta R} \ln\left(\frac{R_{in}}{R_{out}}\right) = 4\pi R_{in}\frac{\mu_\sigma}{\Delta R} \ln\left(\frac{R_{in}}{R_{in}+\Delta R}\right) \tag{S8}$$

where we have used the fact that in atomic units $1/\varepsilon_0 = 4\pi$.

For consistency with the convention in some DFT-codes of calculating the electrostatic potential (Figure 3a) using the (negatively charged) electron as test charge, leading to lower (higher) electrostatic potential for electron-rich (poor) regions, the sign of Eq. S8 needs to be changed leading to:

$$\Delta V = V(R_{in}) - V(R_{out}) = -4\pi R_{in}\frac{\mu_\sigma}{\Delta R}\ln\left(\frac{R_{in}}{R_{out}}\right) = -4\pi R_{in}\frac{\mu_\sigma}{\Delta R}\ln\left(\frac{R_{in}}{R_{in}+\Delta R}\right) \quad \text{(S9)}$$

This correctly describes regions of high (low) electrostatic potential for the electron-rich (poor) side of the NT-cavity (Figure 3a). Eq. S8 allows computation of dipole-density from the step in the electrostatic potential across the NT-wall. Given the solution to the DFT problem via discretized grids,[S3] the non-homogeneous electrostatic potential inside (and immediately outside) any material, and in analogy with standard procedure for planar dipole densities,[S2] it is convenient to angularly and longitudinally average the electrostatic potential (expressed in cylindrical coordinates):

$$\bar{V}(r) = \frac{1}{2\pi L}\int_0^{2\pi} d\phi \int_0^{L} dl\, V(r,\phi,l) \quad \text{(S10)}$$

obtaining:

$$\Delta\bar{V} = \bar{V}(R_{in}) - \bar{V}(R_{out}) = -4\pi R_{in}\frac{\mu_\sigma}{\Delta R}\ln\left(\frac{R_{in}}{R_{out}}\right) = -4\pi R_{in}\frac{\mu_\sigma}{\Delta R}\ln\left(\frac{R_{in}}{R_{in}+\Delta R}\right) \quad \text{(S11)}$$

This last equation is used to compute $\mu_\sigma$ on the basis of the potential step ($\Delta\bar{V}$) between the electrostatically derived $R_{in}$ and $R_{out}$ (Figure 3).

It is worth noting that, for increasingly large $R_{in}$ ($R_{out} = R_{in} + \Delta R$), the cylindrical capacitor asymptotically tends to a planar one, and Eq. S11 asymptotically recovers the established $\frac{\Delta\bar{V}}{\mu_\sigma} = 4\pi$ relationship (Figure S3) for the potential step due to a planar dipole density.[S1]

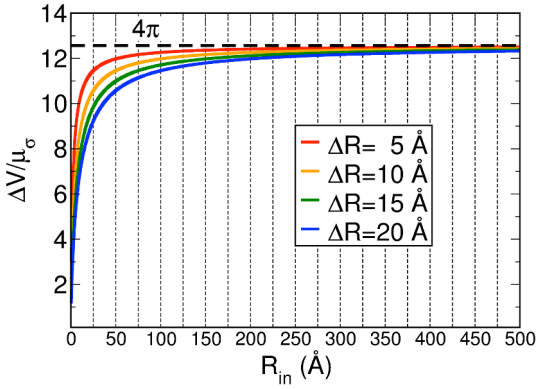



**Figure S3.** Asymptotic behavior of $\frac{\Delta\bar{V}}{\mu_\sigma} = -4\pi\frac{R_{in}}{\Delta R}\ln\left(\frac{R_{in}}{R_{in}+\Delta R}\right)$ (obtained from Eq. S11) for increasing values of $R_{in}$ and $\Delta R$.

Eq. S10 allows exploring the role of the geometric factors and the interplay between $R_{in}$ and $\Delta R$ in damping the relationship between surface dipole-density $\mu_\sigma$ and potential step across the NT-wall $\Delta\bar{V}$. As shown in Figure S4, Large $R_{in}$ and small $\Delta R$ values allow

maximization of the potential difference ( $\Delta\overline{V}$ ) for a given surface dipole-density ( $\mu_\sigma$). Conversely, smaller $\Delta\overline{V}$ values can be obtained for the same $\mu_\sigma$ provided $R_{in}$ ( $\Delta R$ ) is decreased (increased).

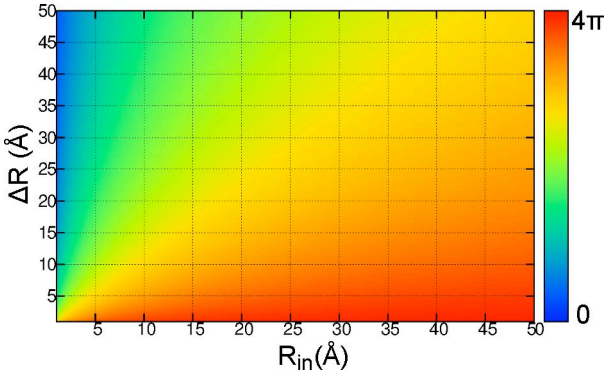



**Figure S4.** Two-dimensional plot of $\frac{\Delta\overline{V}}{\mu_\sigma} = -4\pi\frac{R_{in}}{\Delta R}\ln\left(\frac{R_{in}}{R_{in}+\Delta R}\right)$ (obtained from Eq. S11) as a function of $R_{in}$ and $\Delta R$ .

**Band structure calculations**

Band structure calculations were performed via the Projected Augmented Wave (PAW) method as implemented in the VASP program [S4], with the PBE XC-functional [S5], a 400 eV plane wave energy cutoff, 0.1 eV Gaussian smearing, and 10 k-points along the reciprocal periodic direction of the NTs.

As common practice [S6], effective electron (hole) mass were computed via parabolic fitting at the bottom (top) of the computed conduction (valence) band, with wavevector (**k**) fitting ranges small enough to ensure fitting errors of less than 0.5%.

## 2. Supplementary results

**Table S1.** Average atom-resolved diameters and standard deviation (Å) for the optimized NT-models and considered XC-functionals. The adopted labeling corresponds to the atom element and the subscript-suffix numbers the radial layer (see also Figure 1a). *N* is the number of radially non-equivalent Al-atoms contained within the NT circumference.

| | $H_1$ [Å] | $C_2$ [Å] | $Si_3$ [Å] | $O_4$ [Å] | $Al_5$ [Å] | $O_6$ [Å] | $H_7$ [Å] |
|---|---|---|---|---|---|---|---|
| **N = 24** | | | | | | | |
| PBE | 12.48±0.01 | 13.24±0.01 | 16.90±0.01 | 18.17±0.04 | 20.08±0.01 | 22.25±0.05 | 23.45±0.04 |
| PBE-E | 12.48±0.01 | 13.24±0.01 | 16.90±0.01 | 18.17±0.04 | 20.08±0.01 | 22.25±0.05 | 23.45±0.04 |
| PBE-D2 | 12.48±0.01 | 13.24±0.01 | 16.90±0.01 | 18.17±0.04 | 20.08±0.01 | 22.25±0.05 | 23.45±0.04 |
| VDWDF | 12.48±0.01 | 13.24±0.01 | 16.90±0.01 | 18.17±0.04 | 20.08±0.01 | 22.24±0.05 | 23.46±0.04 |
| OPTPBE | 12.48±0.01 | 13.24±0.01 | 16.90±0.01 | 18.17±0.04 | 20.08±0.01 | 22.24±0.05 | 23.45±0.04 |
| OPTB88 | 12.48±0.01 | 13.24±0.01 | 16.90±0.01 | 18.17±0.04 | 20.08±0.01 | 22.24±0.05 | 23.45±0.04 |
| **N = 26** | | | | | | | |
| PBE | 13.73±0.00 | 14.48±0.00 | 18.15±0.00 | 19.43±0.04 | 21.36±0.00 | 23.54±0.04 | 24.71±0.05 |
| PBE-E | 13.73±0.00 | 14.48±0.00 | 18.15±0.00 | 19.43±0.04 | 21.36±0.00 | 23.54±0.04 | 24.71±0.05 |
| PBE-D2 | 13.73±0.00 | 14.49±0.00 | 18.15±0.00 | 19.43±0.04 | 21.36±0.00 | 23.53±0.04 | 24.71±0.05 |
| VDWDF | 13.73±0.00 | 14.49±0.00 | 18.15±0.00 | 19.43±0.04 | 21.37±0.00 | 23.53±0.04 | 24.72±0.05 |
| OPTPBE | 13.73±0.00 | 14.50±0.00 | 18.16±0.00 | 19.44±0.04 | 21.36±0.00 | 23.53±0.04 | 24.72±0.05 |
| OPTB88 | 13.73±0.00 | 14.50±0.00 | 18.16±0.00 | 19.43±0.04 | 21.36±0.00 | 23.52±0.04 | 24.71±0.04 |
| **N = 28** | | | | | | | |
| PBE | 15.33±0.03 | 16.10±0.02 | 19.77±0.01 | 21.04±0.04 | 22.97±0.01 | 25.15±0.05 | 26.33±0.03 |
| PBE-E | 15.33±0.03 | 16.10±0.02 | 19.77±0.01 | 21.04±0.04 | 22.97±0.01 | 25.15±0.05 | 26.33±0.03 |
| PBE-D2 | 15.35±0.01 | 16.11±0.01 | 19.78±0.00 | 21.04±0.04 | 22.97±0.01 | 25.14±0.04 | 26.32±0.02 |
| VDWDF | 15.34±0.01 | 16.11±0.01 | 19.78±0.01 | 21.05±0.03 | 22.98±0.01 | 25.14±0.04 | 26.35±0.03 |
| OPTPBE | 15.34±0.02 | 16.11±0.01 | 19.77±0.01 | 21.04±0.03 | 22.97±0.01 | 25.14±0.04 | 26.33±0.03 |
| OPTB88 | 15.34±0.02 | 16.11±0.01 | 19.78±0.01 | 21.04±0.03 | 22.97±0.01 | 25.13±0.04 | 26.33±0.03 |
| **N = 30** | | | | | | | |
| PBE | 16.93±0.02 | 17.68±0.01 | 21.35±0.00 | 22.61±0.05 | 24.55±0.00 | 26.72±0.04 | 27.90±0.05 |
| PBE-E | 16.93±0.01 | 17.70±0.01 | 21.39±0.01 | 22.64±0.03 | 24.58±0.01 | 26.76±0.04 | 27.95±0.02 |
| PBE-D2 | 16.94±0.01 | 17.69±0.01 | 21.36±0.00 | 22.61±0.04 | 24.54±0.00 | 26.71±0.04 | 27.88±0.04 |
| VDWDF | 16.97±0.02 | 17.74±0.02 | 21.42±0.02 | 22.67±0.04 | 24.61±0.02 | 26.77±0.04 | 27.98±0.03 |
| OPTPBE | 16.96±0.02 | 17.73±0.02 | 21.41±0.02 | 22.65±0.04 | 24.58±0.02 | 26.75±0.04 | 27.94±0.03 |
| OPTB88 | 16.93±0.01 | 17.69±0.01 | 21.35±0.00 | 22.61±0.05 | 24.53±0.00 | 26.70±0.04 | 27.89±0.05 |
| **N = 32** | | | | | | | |
| PBE | 18.55±0.02 | 19.32±0.02 | 23.01±0.01 | 24.26±0.03 | 26.19±0.01 | 28.37±0.04 | 29.56±0.03 |
| PBE-E | 18.53±0.02 | 19.30±0.02 | 22.99±0.01 | 24.24±0.03 | 26.18±0.01 | 28.36±0.04 | 29.55±0.01 |
| PBE-D2 | 18.53±0.03 | 19.29±0.02 | 22.96±0.00 | 24.20±0.05 | 26.14±0.01 | 28.32±0.04 | 29.49±0.06 |
| VDWDF | 18.55±0.02 | 19.32±0.02 | 23.01±0.02 | 24.26±0.04 | 26.20±0.02 | 28.36±0.04 | 29.56±0.02 |
| OPTPBE | 18.56±0.02 | 19.32±0.02 | 23.00±0.01 | 24.24±0.04 | 26.16±0.02 | 28.33±0.04 | 29.52±0.02 |
| OPTB88 | 18.54±0.05 | 19.30±0.02 | 22.96±0.00 | 24.21±0.05 | 26.13±0.01 | 28.30±0.03 | 29.50±0.05 |
| **N = 34** | | | | | | | |
| PBE | 20.11±0.01 | 20.88±0.01 | 24.56±0.01 | 25.79±0.04 | 27.73±0.01 | 29.91±0.03 | 31.07±0.04 |
| PBE-E | 20.12±0.01 | 20.88±0.01 | 24.56±0.01 | 25.79±0.04 | 27.73±0.01 | 29.90±0.03 | 31.07±0.04 |
| PBE-D2 | 20.11±0.01 | 20.87±0.01 | 24.56±0.01 | 25.80±0.03 | 27.73±0.01 | 29.90±0.03 | 31.07±0.04 |
| VDWDF | 20.10±0.01 | 20.87±0.01 | 24.56±0.01 | 25.80±0.03 | 27.74±0.01 | 29.91±0.03 | 31.10±0.04 |
| OPTPBE | 20.12±0.01 | 20.88±0.01 | 24.56±0.01 | 25.80±0.04 | 27.73±0.01 | 29.90±0.03 | 31.08±0.04 |
| OPTB88 | 20.12±0.01 | 20.89±0.01 | 24.56±0.01 | 25.80±0.04 | 27.72±0.01 | 29.89±0.03 | 31.07±0.04 |
| **N = 36** | | | | | | | |
| PBE | 21.69±0.02 | 22.46±0.01 | 26.15±0.01 | 27.38±0.04 | 29.32±0.01 | 31.50±0.04 | 32.70±0.05 |
| PBE-E | 21.69±0.02 | 22.46±0.01 | 26.15±0.01 | 27.38±0.04 | 29.32±0.01 | 31.50±0.04 | 32.70±0.05 |
| PBE-D2 | 21.72±0.00 | 22.48±0.01 | 26.16±0.01 | 27.38±0.04 | 29.32±0.01 | 31.49±0.03 | 32.67±0.03 |
| VDWDF | 21.70±0.01 | 22.47±0.01 | 26.15±0.01 | 27.39±0.03 | 29.33±0.01 | 31.50±0.03 | 32.71±0.04 |
| OPTPBE | 21.71±0.01 | 22.48±0.01 | 26.16±0.01 | 27.39±0.04 | 29.32±0.01 | 31.49±0.03 | 32.70±0.04 |
| OPTB88 | 21.70±0.01 | 22.47±0.01 | 26.15±0.01 | 27.39±0.04 | 29.32±0.01 | 31.48±0.03 | 32.70±0.05 |

**Table S2.** Average Layer-resolved bond lengths and their standard deviations (Å) for optimized NT-models and considered XC-functionals. The adopted labeling corresponds to the atom element and the subscript-suffix numbers the radial layer (see also Figure 1a). *N* is the number of radially non-equivalent Al-atoms in the NT circumference. The PBE results for the pristine $AlSi_{24}$ NT are reported for comparison.

| | $H_1$-$C(O)_2$ [Å] | $C(O)_2$-$Si(Ge)_3$ [Å] | $Si(Ge)_3$-$O_4$ [Å] | $O_4$-$Al_5$ [Å] | $Al_5$-$O_6$ [Å] | $O_6$-$H_7$ [Å] |
|---|---|---|---|---|---|---|
| **$AlSi_{24}$ (PBE)** | 0.97±0.00 | 1.65±0.00 | 1.65±0.01 | 1.94±0.02 | 1.89±0.01 | 0.96±0.00 |
| **N = 24** | | | | | | |
| PBE | 1.09±0.00 | 1.84±0.00 | 1.66±0.01 | 1.95±0.01 | 1.90±0.01 | 0.96±0.00 |
| PBE-E | 1.09±0.00 | 1.84±0.00 | 1.66±0.01 | 1.95±0.01 | 1.90±0.01 | 0.96±0.00 |
| PBE-D2 | 1.09±0.00 | 1.84±0.00 | 1.66±0.01 | 1.95±0.01 | 1.90±0.01 | 0.96±0.00 |
| VDWDF | 1.08±0.00 | 1.84±0.00 | 1.66±0.01 | 1.95±0.01 | 1.90±0.01 | 0.96±0.00 |
| OPTPBE | 1.09±0.00 | 1.84±0.00 | 1.66±0.01 | 1.95±0.01 | 1.90±0.01 | 0.96±0.00 |
| OPTB88 | 1.09±0.00 | 1.84±0.00 | 1.66±0.01 | 1.95±0.01 | 1.90±0.01 | 0.96±0.00 |
| **N = 26** | | | | | | |
| PBE | 1.09±0.00 | 1.85±0.00 | 1.66±0.01 | 1.94±0.01 | 1.89±0.01 | 0.96±0.00 |
| PBE-E | 1.09±0.00 | 1.85±0.00 | 1.66±0.01 | 1.94±0.01 | 1.89±0.01 | 0.96±0.00 |
| PBE-D2 | 1.09±0.00 | 1.85±0.00 | 1.66±0.01 | 1.94±0.01 | 1.89±0.01 | 0.96±0.00 |
| VDWDF | 1.08±0.00 | 1.83±0.00 | 1.66±0.01 | 1.95±0.01 | 1.89±0.01 | 0.96±0.00 |
| OPTPBE | 1.09±0.00 | 1.85±0.00 | 1.66±0.01 | 1.94±0.01 | 1.89±0.01 | 0.96±0.00 |
| OPTB88 | 1.09±0.00 | 1.84±0.00 | 1.66±0.01 | 1.94±0.01 | 1.89±0.01 | 0.96±0.00 |
| **N = 28** | | | | | | |
| PBE | 1.09±0.00 | 1.85±0.00 | 1.66±0.01 | 1.94±0.01 | 1.89±0.01 | 0.96±0.00 |
| PBE-E | 1.09±0.00 | 1.85±0.00 | 1.66±0.01 | 1.94±0.01 | 1.89±0.01 | 0.96±0.00 |
| PBE-D2 | 1.09±0.00 | 1.85±0.00 | 1.66±0.01 | 1.94±0.01 | 1.89±0.01 | 0.96±0.00 |
| VDWDF | 1.09±0.00 | 1.85±0.00 | 1.66±0.01 | 1.95±0.01 | 1.89±0.01 | 0.96±0.00 |
| OPTPBE | 1.09±0.00 | 1.85±0.00 | 1.66±0.01 | 1.94±0.01 | 1.89±0.01 | 0.96±0.00 |
| OPTB88 | 1.09±0.00 | 1.85±0.00 | 1.66±0.01 | 1.94±0.01 | 1.89±0.01 | 0.96±0.00 |
| **N = 30** | | | | | | |
| PBE | 1.09±0.00 | 1.85±0.00 | 1.66±0.01 | 1.95±0.01 | 1.89±0.01 | 0.96±0.00 |
| PBE-E | 1.09±0.00 | 1.85±0.00 | 1.66±0.01 | 1.95±0.01 | 1.89±0.01 | 0.96±0.00 |
| PBE-D2 | 1.09±0.00 | 1.85±0.00 | 1.66±0.01 | 1.94±0.01 | 1.89±0.01 | 0.96±0.00 |
| VDWDF | 1.09±0.00 | 1.85±0.00 | 1.66±0.01 | 1.95±0.01 | 1.89±0.01 | 0.96±0.00 |
| OPTPBE | 1.09±0.00 | 1.85±0.00 | 1.66±0.01 | 1.95±0.01 | 1.89±0.01 | 0.96±0.00 |
| OPTB88 | 1.09±0.00 | 1.85±0.00 | 1.66±0.01 | 1.94±0.01 | 1.89±0.01 | 0.96±0.00 |
| **N = 32** | | | | | | |
| PBE | 1.09±0.00 | 1.85±0.00 | 1.67±0.00 | 1.95±0.01 | 1.89±0.01 | 0.96±0.00 |
| PBE-E | 1.09±0.00 | 1.85±0.00 | 1.67±0.01 | 1.95±0.01 | 1.89±0.01 | 0.96±0.00 |
| PBE-D2 | 1.09±0.00 | 1.85±0.00 | 1.67±0.01 | 1.95±0.01 | 1.89±0.01 | 0.96±0.00 |
| VDWDF | 1.09±0.00 | 1.85±0.00 | 1.66±0.01 | 1.95±0.01 | 1.89±0.01 | 0.96±0.00 |
| OPTPBE | 1.09±0.00 | 1.85±0.00 | 1.66±0.01 | 1.95±0.01 | 1.89±0.01 | 0.96±0.00 |
| OPTB88 | 1.09±0.00 | 1.85±0.00 | 1.66±0.01 | 1.95±0.01 | 1.88±0.01 | 0.96±0.00 |
| **N = 34** | | | | | | |
| PBE | 1.09±0.00 | 1.85±0.00 | 1.67±0.00 | 1.95±0.01 | 1.88±0.01 | 0.96±0.00 |
| PBE-E | 1.09±0.00 | 1.85±0.00 | 1.67±0.00 | 1.95±0.01 | 1.88±0.01 | 0.96±0.00 |
| PBE-D2 | 1.09±0.00 | 1.85±0.00 | 1.67±0.01 | 1.95±0.01 | 1.89±0.01 | 0.96±0.00 |
| VDWDF | 1.09±0.00 | 1.85±0.00 | 1.66±0.01 | 1.95±0.01 | 1.89±0.01 | 0.96±0.00 |
| OPTPBE | 1.09±0.00 | 1.85±0.00 | 1.66±0.01 | 1.95±0.01 | 1.88±0.01 | 0.96±0.00 |
| OPTB88 | 1.09±0.00 | 1.84±0.00 | 1.66±0.00 | 1.95±0.01 | 1.88±0.01 | 0.96±0.00 |
| **N = 36** | | | | | | |
| PBE | 1.09±0.00 | 1.85±0.00 | 1.67±0.00 | 1.95±0.01 | 1.88±0.01 | 0.96±0.00 |
| PBE-E | 1.09±0.00 | 1.85±0.00 | 1.67±0.00 | 1.95±0.01 | 1.88±0.01 | 0.96±0.00 |
| PBE-D2 | 1.09±0.00 | 1.85±0.00 | 1.67±0.01 | 1.95±0.01 | 1.89±0.01 | 0.96±0.00 |
| VDWDF | 1.09±0.00 | 1.85±0.00 | 1.67±0.01 | 1.95±0.01 | 1.88±0.01 | 0.96±0.00 |
| OPTPBE | 1.09±0.00 | 1.85±0.00 | 1.67±0.01 | 1.95±0.01 | 1.88±0.01 | 0.96±0.00 |
| OPTB88 | 1.09±0.00 | 1.85±0.00 | 1.67±0.01 | 1.95±0.01 | 1.88±0.01 | 0.96±0.00 |

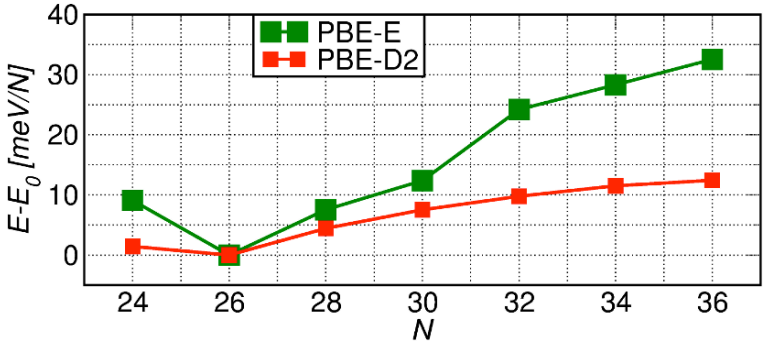



**Figure S5.** Relative dispersion energy normalized to the number of Al-atoms in the NT (*N*), and referenced to the computed minimum, for the PBE-D2 and PBE-E XC-functionals.

**Table S3.** Vacuum-aligned valence (VBEs) and conduction band edges (CBEs), and resulting band gaps (BGs)of the simulated NTs for increasing number of Al-atoms in the circumference (N) and the adopted XC-functionals.

| N | PBE [eV] | PBE-E [eV] | PBE-D2 [eV] | VDWDF [eV] | OPTPBE [eV] | OPTB88 [eV] |
|---|---|---|---|---|---|---|
| **VBEs** | | | | | | |
| **24** | -5.91 | -5.91 | -5.91 | -6.17 | -6.14 | -6.15 |
| **26** | -5.97 | -5.97 | -5.98 | -6.14 | -6.21 | -6.17 |
| **28** | -5.97 | -5.97 | -5.96 | -6.16 | -6.19 | -6.21 |
| **30** | -5.96 | -5.91 | -5.97 | -6.14 | -6.15 | -6.21 |
| **32** | -5.92 | -5.90 | -5.96 | -6.13 | -6.15 | -6.21 |
| **34** | -5.97 | -5.96 | -5.97 | -6.18 | -6.20 | -6.24 |
| **36** | -5.88 | -5.89 | -5.92 | -6.11 | -6.09 | -6.14 |
| **CBEs** | | | | | | |
| **24** | -1.20 | -1.20 | -1.20 | -1.69 | -1.69 | -1.52 |
| **26** | -1.23 | -1.23 | -1.23 | -1.70 | -1.72 | -1.49 |
| **28** | -1.22 | -1.22 | -1.24 | -1.70 | -1.71 | -1.55 |
| **30** | -1.23 | -1.19 | -1.25 | -1.70 | -1.71 | -1.55 |
| **32** | -1.10 | -1.19 | -1.23 | -1.70 | -1.72 | -1.55 |
| **34** | -1.24 | -1.24 | -1.26 | -1.71 | -1.73 | -1.56 |
| **36** | -1.19 | -1.19 | -1.24 | -1.69 | -1.69 | -1.52 |
| **BGs** | | | | | | |
| **24** | 4.71 | 4.71 | 4.72 | 4.48 | 4.45 | 4.64 |
| **26** | 4.74 | 4.74 | 4.75 | 4.44 | 4.49 | 4.68 |
| **28** | 4.75 | 4.75 | 4.72 | 4.46 | 4.48 | 4.67 |
| **30** | 4.73 | 4.73 | 4.71 | 4.44 | 4.44 | 4.66 |
| **32** | 4.72 | 4.71 | 4.73 | 4.43 | 4.43 | 4.66 |
| **34** | 4.73 | 4.72 | 4.71 | 4.47 | 4.47 | 4.68 |
| **36** | 4.70 | 4.70 | 4.68 | 4.42 | 4.40 | 4.62 |

**Table S4.** PBE Vacuum-aligned valence (VBEs) and conduction band edges (CBEs), and resulting band gaps (BGs) for the minimum-energy $AlSi_N$-Me (N=28, 30) NTs optimized at VDWDF, OPTPBE and OPTB88 level. For ease of comparison the VDWDF, OPTPBE and OPTB88 values on the same geometries (from Table S3) have been reported within brackets.

| N | XC-funtional for geometry opimization | VBEs [eV] | CBEs [eV] | BGs [eV] |
|---|---|---|---|---|
| **28** | **PBE** | -5.97 | -1.22 | 4.75 |
| **28** | **OPTB88** | -5.92 (-6.21) | -1.20 (-1.55) | 4.72 (4.67) |
| **30** | **PBE** | -5.96 | -1.23 | 4.73 |
| **30** | **VDWDF** | -5.84 (-6.14) | -1.19 (-1.70) | 4.66 (4.44) |
| **30** | **OPTPBE** | -5.89 (-6.15) | -1.22 (-1.71) | 4.67 (4.44) |
| **30** | **OPTB88** | -5.91 (-6.21) | -1.21 (-1.55) | 4.70 (4.66) |

**Table S5.** Muliken charges (e) for the methyl groups ($C_2$,$H_1$) at the NT inner surface for each of the XC-functionals considered.

| N | PBE [e] | PBE-E [e] | PBE-D2 [e] | VDWDF [e] | OPTPBE [e] | OPTB88 [e] |
|---|---|---|---|---|---|---|
| **24** | -0.3076 | -0.3080 | -0.3086 | -0.3184 | -0.3129 | -0.3197 |
| **26** | -0.3013 | -0.3012 | -0.3024 | -0.3115 | -0.3067 | -0.3128 |
| **28** | -0.2934 | -0.2933 | -0.2938 | -0.3088 | -0.2990 | -0.3109 |
| **30** | -0.2876 | -0.2896 | -0.2856 | -0.3022 | -0.2961 | -0.2985 |
| **32** | -0.2818 | -0.2838 | -0.2833 | -0.2986 | -0.2889 | -0.2938 |
| **34** | -0.2720 | -0.2730 | -0.2765 | -0.2942 | -0.2816 | -0.2919 |
| **36** | -0.2753 | -0.2758 | -0.2729 | -0.2932 | -0.2836 | -0.2884 |



**Figure S6.** Front view of the (PBE) optimized $AlSi_{24}$-Me ($Fe_2$-$AlSi_{24}$-Me, left) and $AlSi_{36}$-Me ($Fe_2$-$AlSi_{36}$-Me, right) NTs with two (octahedral) Fe atoms substituted to two Al atoms. Same coloring scheme as in Figure 1, with the additional Fe atoms being colored orange.

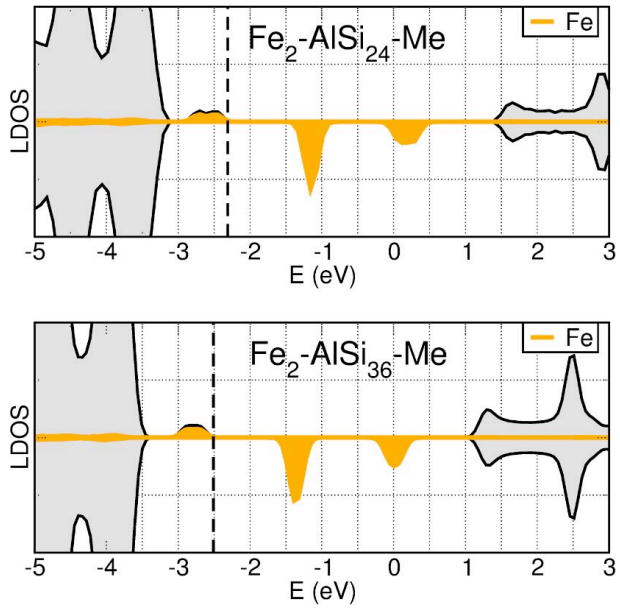



**Figure S7.** PBE total DOS (filled grey) and Fe-resolved LDOS (filled orange) plots for energy-favored ferromagnetic high-spin ordering of the Fe-doped NTs in Fig. S6. The dashed vertical line marks the position of the high-energy end of the occupied (L)DOS peak corresponding to Fe-dopant band gap states. At odds with results in Ref. [14f] for hydroxylated (not methylated) NTs with different XC-functionals (PW91, BLYP, B3LYP), high-spin (magnetic moment per Fe-atom: 3.7 $\mu_B$) ferromagnetic ordering is computed to be favored by more than 1.3 eV and 1.6 eV eV over ferromagnetic low-spin (magnetic moment per Fe-atom: 1 $\mu_B$) and anti-ferromagnetic (magnetic moment per Fe-atom: ±1 $\mu_B$) solutions, respectively. The absence of details on whether different magnetic solutions were explored and converged in Ref. [14f] prevents further elaboration on these deviations.

**Table S6.** Computed surface dipole density ($\mu_\sigma$), potential difference between inner and outer vacuum plateaus ($\Delta\overline{V}$), and electrostatically derived inner ($R_{in}$) and outer ($R_{out}$) NT radii for the considered models and XC-functionals. The PBE results for the pristine $AlSi_{24}$ NT are reported for comparison.

| | $\mu_\sigma$ [pC m$^{-1}$] | $\Delta\overline{V}$ [eV] | $R_{in}$ [Å] | $R_{out}$ [Å] |
|---|---|---|---|---|
| **$AlSi_{24}$ (PBE)** | 22.48 | 1.40 | 4.52 | 13.45 |
| ***N* = 24** | | | | |
| PBE | 14.24 | 0.84 | 4.17 | 13.57 |
| PBE-E | 14.24 | 0.84 | 4.17 | 13.57 |
| PBE-D2 | 14.05 | 0.83 | 4.17 | 13.57 |
| VdWDF | 14.87 | 0.88 | 4.17 | 13.57 |
| OPTPBE | 15.10 | 0.89 | 4.17 | 13.57 |
| OPTB88 | 15.34 | 0.92 | 4.17 | 13.56 |
| ***N* = 26** | | | | |
| PBE | 12.38 | 0.77 | 4.76 | 14.28 |
| PBE-E | 12.40 | 0.77 | 4.76 | 14.28 |
| PBE-D2 | 12.14 | 0.75 | 4.76 | 14.28 |
| VdWDF | 14.75 | 0.92 | 4.88 | 14.40 |
| OPTPBE | 13.00 | 0.80 | 4.76 | 14.28 |
| OPTB88 | 13.23 | 0.82 | 4.76 | 14.28 |
| ***N* = 28** | | | | |
| PBE | 11.88 | 0.78 | 5.59 | 15.11 |
| PBE-E | 11.92 | 0.78 | 5.59 | 15.11 |
| PBE-D2 | 12.22 | 0.81 | 5.59 | 14.99 |
| VdWDF | 13.66 | 0.90 | 5.59 | 15.11 |
| OPTPBE | 12.76 | 0.84 | 5.59 | 15.11 |
| OPTB88 | 12.87 | 0.85 | 5.59 | 15.11 |
| ***N* = 30** | | | | |
| PBE | 11.53 | 0.85 | 6.42 | 15.23 |
| PBE-E | 12.11 | 0.85 | 6.42 | 15.71 |
| PBE-D2 | 11.49 | 0.80 | 6.42 | 15.82 |
| VdWDF | 13.32 | 0.92 | 6.43 | 15.94 |
| OPTPBE | 12.85 | 0.89 | 6.42 | 15.94 |
| OPTB88 | 12.38 | 0.86 | 6.42 | 15.82 |
| ***N* = 32** | | | | |
| PBE | 11.65 | 0.85 | 7.38 | 16.66 |
| PBE-E | 11.88 | 0.87 | 7.37 | 16.66 |
| PBE-D2 | 11.24 | 0.81 | 7.14 | 16.66 |
| VdWDF | 13.12 | 0.94 | 7.14 | 16.66 |
| OPTPBE | 12.55 | 0.90 | 7.14 | 16.66 |
| OPTB88 | 12.16 | 0.87 | 7.14 | 16.66 |
| ***N* = 34** | | | | |
| PBE | 10.91 | 0.82 | 8.09 | 17.37 |
| PBE-E | 11.03 | 0.83 | 8.09 | 17.37 |
| PBE-D2 | 10.74 | 0.81 | 8.09 | 17.37 |
| VdWDF | 11.93 | 0.89 | 8.09 | 17.49 |
| OPTPBE | 11.44 | 0.86 | 7.97 | 17.49 |
| OPTB88 | 11.30 | 0.85 | 8.09 | 17.49 |
| ***N* = 36** | | | | |
| PBE | 11.66 | 0.89 | 8.67 | 18.18 |
| PBE-E | 11.62 | 0.89 | 8.67 | 18.18 |
| PBE-D2 | 11.46 | 0.87 | 8.67 | 18.18 |
| VdWDF | 12.82 | 0.98 | 8.67 | 18.18 |
| OPTPBE | 12.73 | 0.97 | 8.67 | 18.18 |
| OPTB88 | 12.28 | 0.94 | 8.67 | 18.18 |

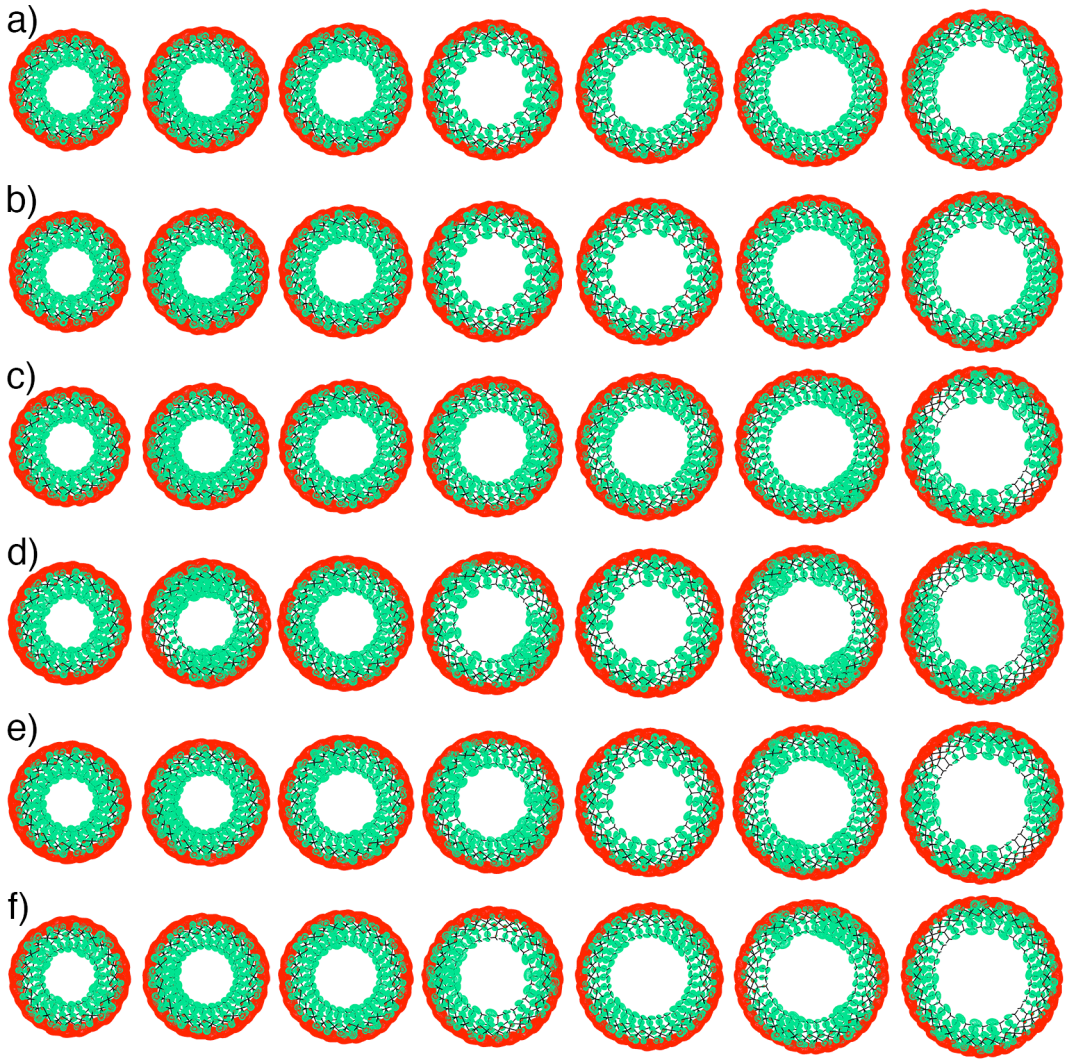



**Figure S8.** Real space separation of the VBE (green) and CBE (red) edges for the considered $AlSi_N$-Me NTs in the N=24 (left)-N=36 (right) range as a function of the XC-functional used. a) PBE, b) PBE-E, c) PBE-D2, d) VDWDF, e) OPTPBE, f) OPTB88. Regardless of the adopted XC-functional, the modelled VB-CB separation is qualitatively unaffected.

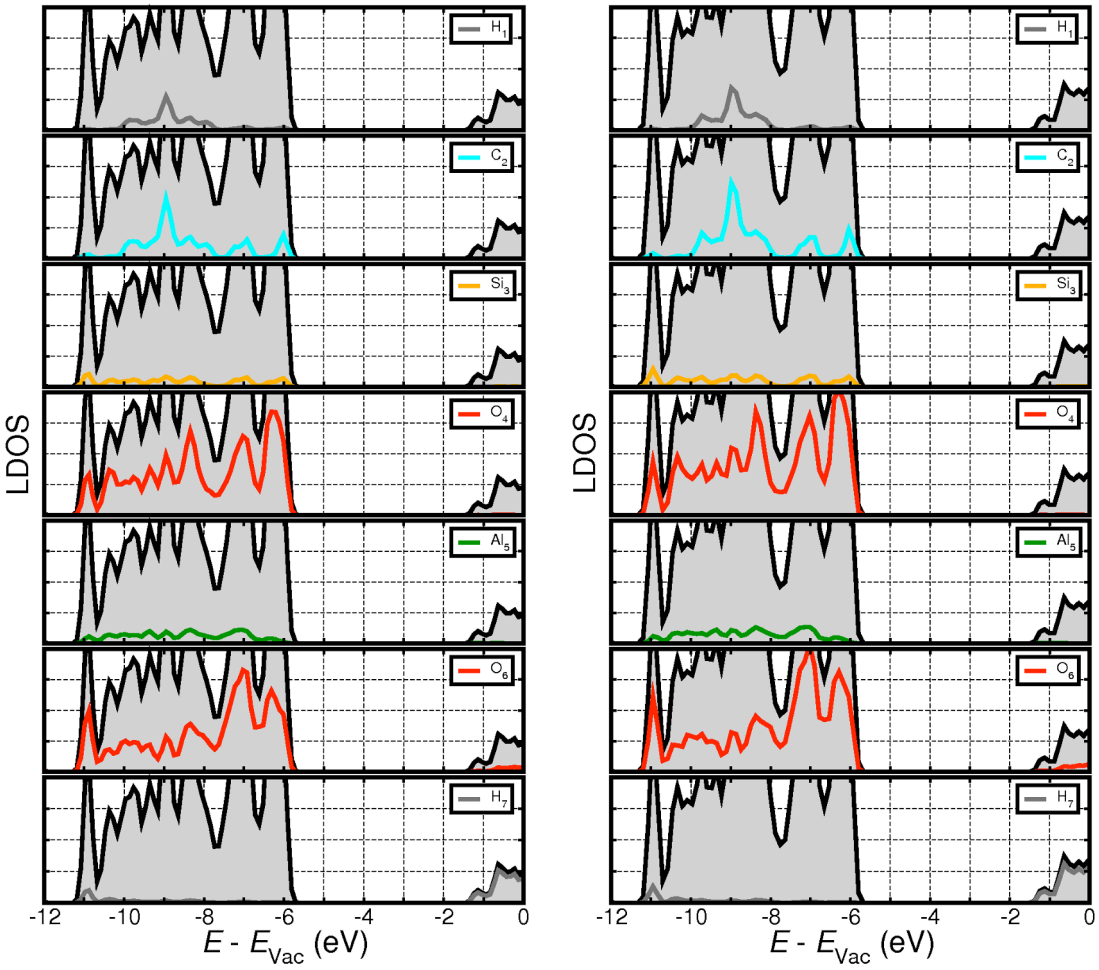



**Figure S9.** Vacuum-aligned **PBE** total DOS plot (filled grey) and layer resolved LDOS plots for the $AlSi_{28}$-Me (left) and $AlSi_{34}$-Me (right) NTs. See Figure 1a for the adopted layer-labeling.

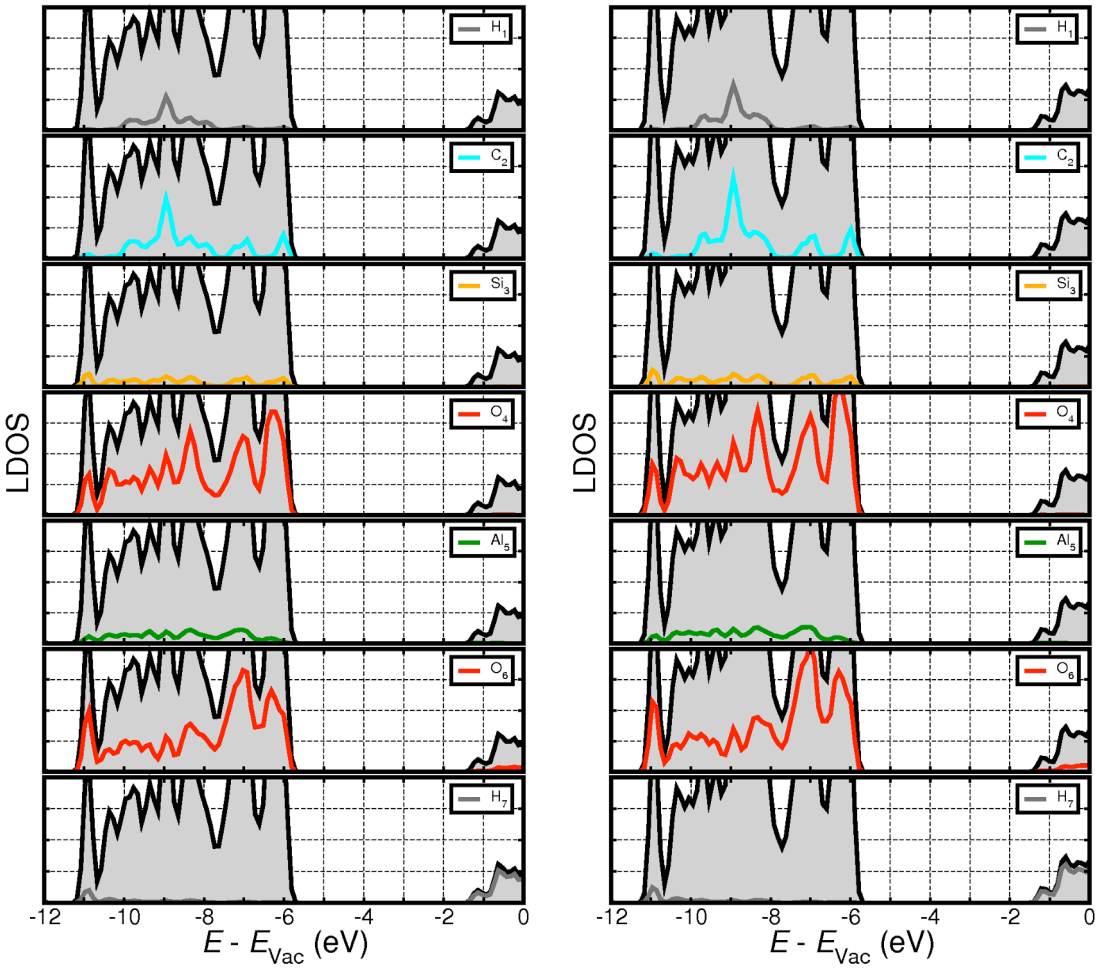



**Figure S10.** Vacuum-aligned **PBE-E** total DOS plot (filled grey) and layer resolved LDOS plots for the $AlSi_{28}$-Me (left) and $AlSi_{34}$-Me (right) NTs. See Figure 1a for the adopted layer-labeling.

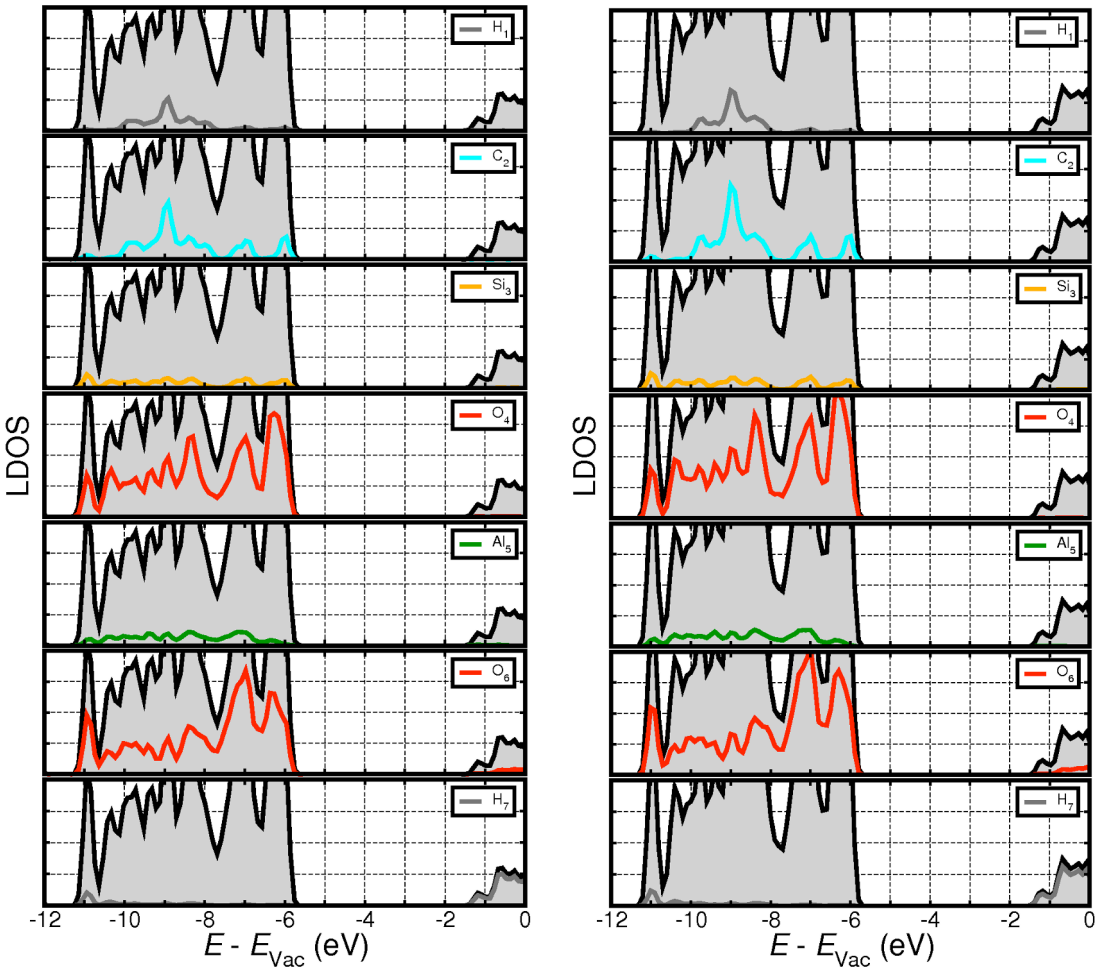



**Figure S11.** Vacuum-aligned **PBE-D2** total DOS plot (filled grey) and layer resolved LDOS plots for the $AlSi_{28}$-Me (left) and $AlSi_{34}$-Me (right) NTs. See Figure 1a for the adopted layer-labeling.

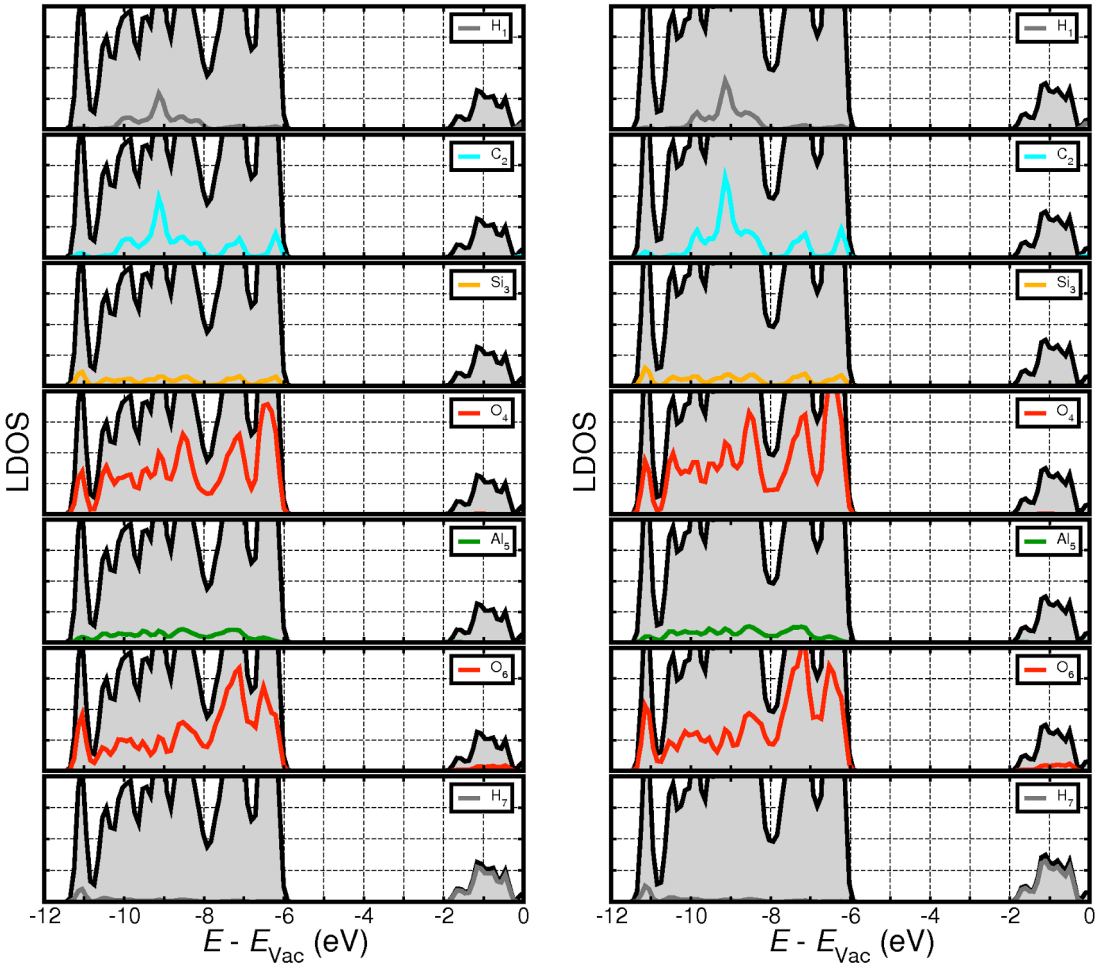



**Figure S12.** Vacuum-aligned **VDWDF** total DOS plot (filled grey) and layer resolved LDOS plots for the $AlSi_{28}$-Me (left) and $AlSi_{34}$-Me (right) NTs. See Figure 1a for the adopted layer-labeling.

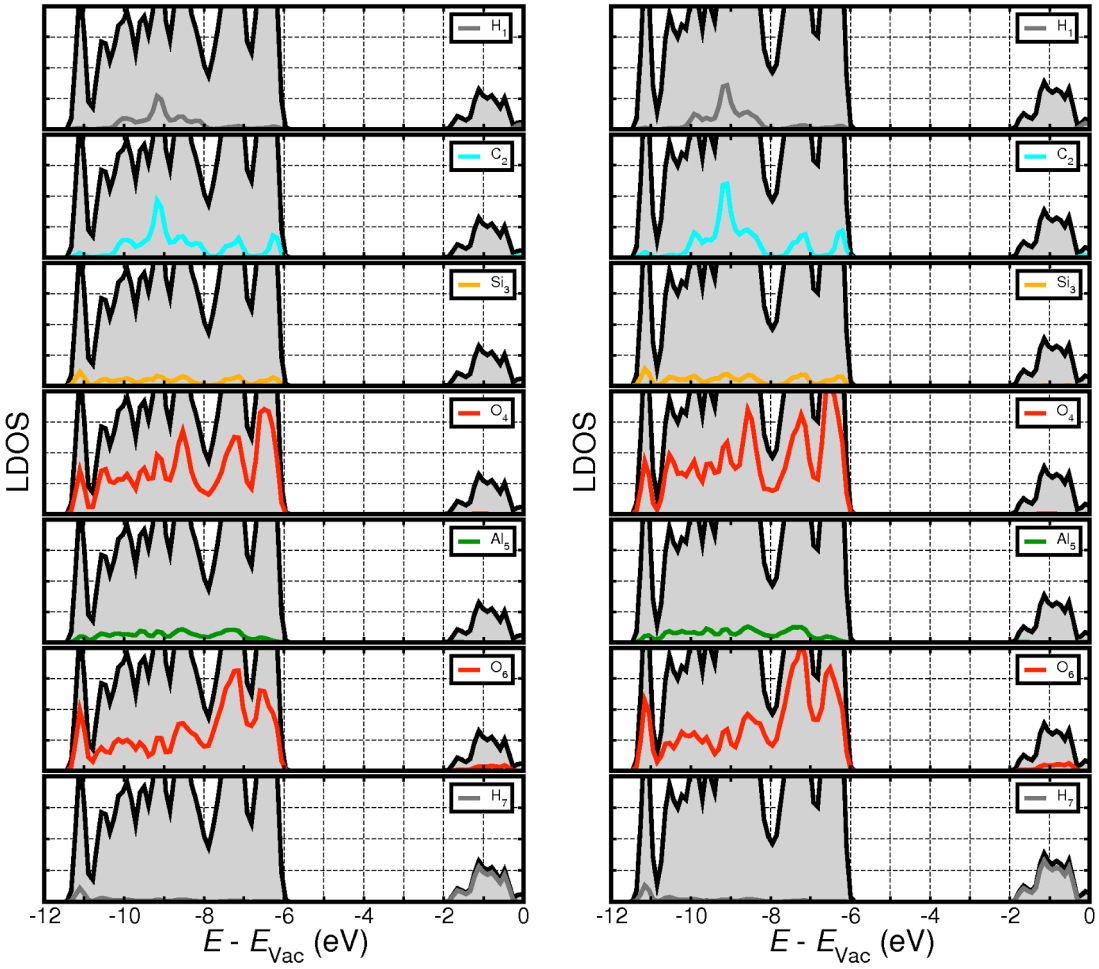



**Figure S13.** Vacuum-aligned **OPTPBE** total DOS plot (filled grey) and layer resolved LDOS plots for the $AlSi_{28}$-Me (left) and $AlSi_{34}$-Me (right) NTs. See Figure 1a for the adopted layer-labeling.

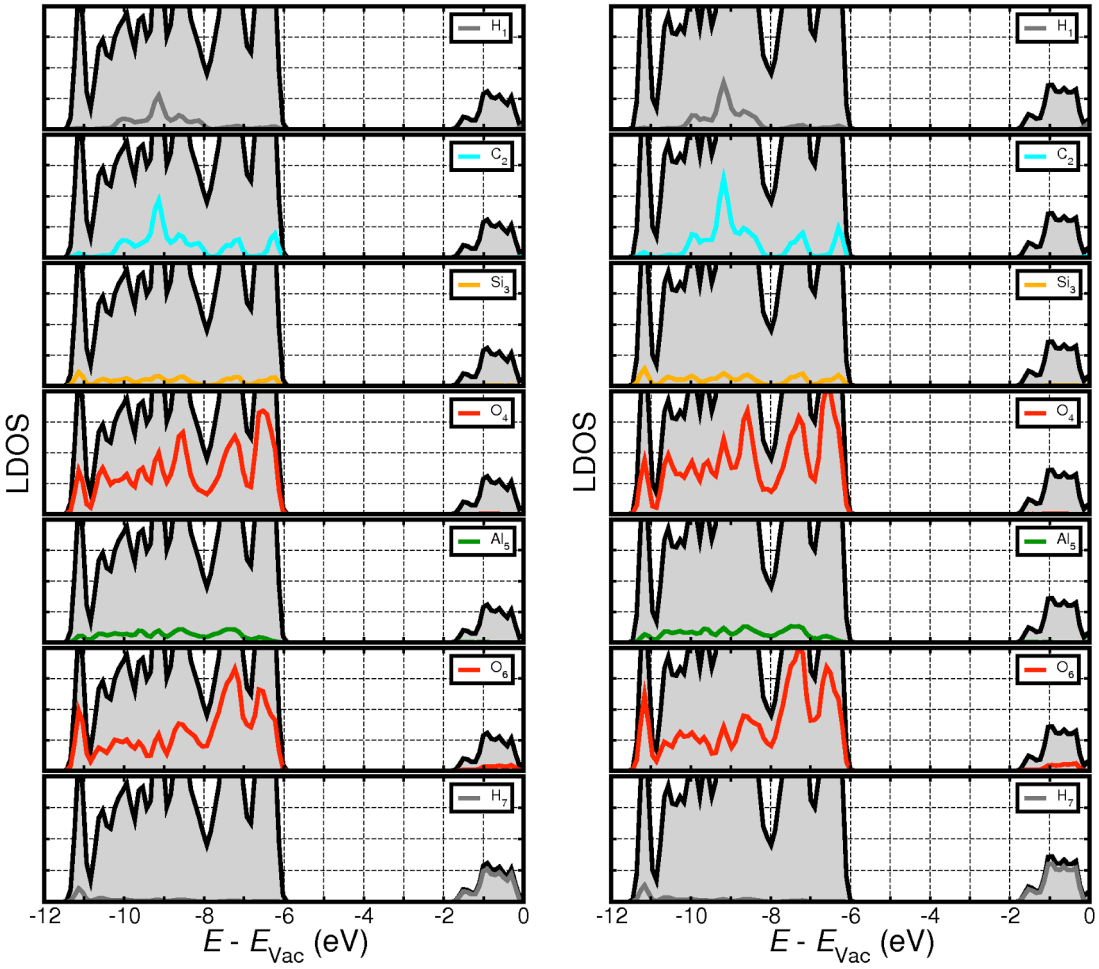



**Figure S14.** Vacuum-aligned **OPTB88** total DOS plot (filled grey) and layer resolved LDOS plots for the $AlSi_{28}$-Me (left) and $AlSi_{34}$-Me (right) NTs. See Figure 1a for the adopted layer-labeling.

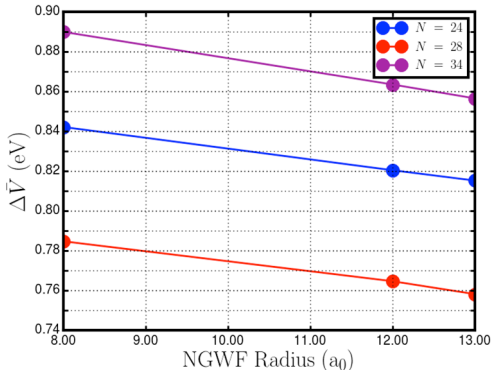



**Figure S15.** The calculated difference in the radially averaged electrostatic plateau inside and outside the NT cavity ($\Delta\bar{V}$) as a function of NGWF radius (bohr, $a_0$) for NTs containing 24, 28 and 36 Al-atoms within their circumference.

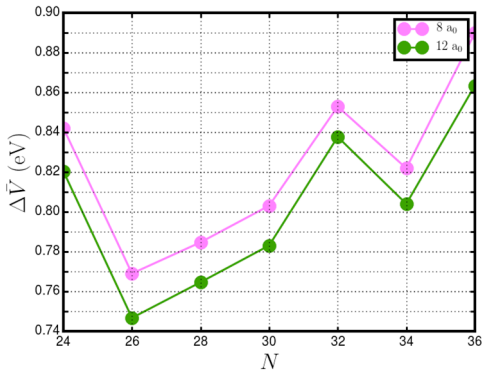



**Figure S16.** The calculated difference in the radially averaged electrostatic plateau inside and outside the NT cavity ($\Delta\bar{V}$) as a function of the number of Al-atoms within the tube circumference for 8 $a_0$ (purple) and 12 $a_0$ (green) NGWFs.

**Table S7.** The calculated potential difference between inner and outer vacuum plateau ($\Delta\overline{V}$), surface dipole density ($\mu_\sigma$), and polarization ($P$) for $AlSi_{24}$-Me, $AlSi_{28}$-Me and $AlSi_{36}$-Me NTs as a function of the psinc basis set kinetic energy cutoff ($E_c$, in eV) and NGWFs radius (R, in Bohr, $a_0$).

| System | $E_c$ [eV] | R [Å] | $\Delta\overline{V}$ [eV] | $\mu_\sigma$ [pC m$^{-1}$] | $P$ [C m$^{-2}$] |
|---|---|---|---|---|---|
| **N=24** | | | | | |
| | 800 | 12 | 0.8186 | 14.006 | 0.01463 |
| | 1000 | 8 | 0.8438 | 14.267 | 0.01520 |
| | 1000 | 12 | 0.8204 | 13.870 | 0.01477 |
| | 1000 | 13 | 0.8152 | 13.782 | 0.01468 |
| **N=28** | | | | | |
| | 1000 | 8 | 0.7884 | 11.942 | 0.01256 |
| | 1000 | 12 | 0.7649 | 11.585 | 0.01219 |
| | 1000 | 13 | 0.7581 | 11.482 | 0.01208 |
| | 1500 | 8 | 0.7888 | 11.710 | 0.01274 |
| **N=36** | | | | | |
| | 1000 | 8 | 0.8866 | 11.614 | 0.0122 |
| | 1000 | 12 | 0.8635 | 11.311 | 0.0119 |
| | 1000 | 13 | 0.8564 | 11.220 | 0.0118 |

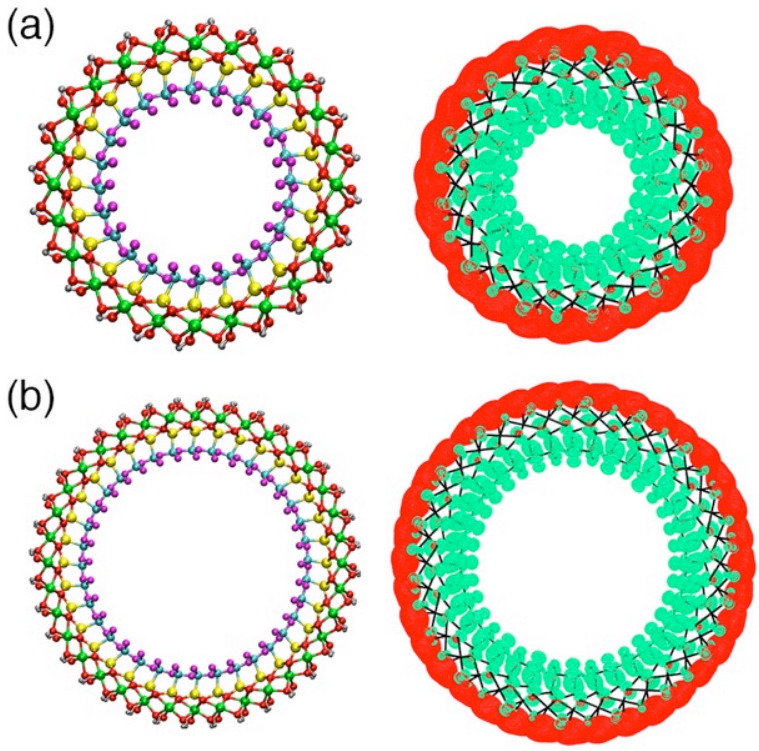



**Figure S17.** The PBE optimized geometry (left) and real-space separation (right) between the VBE (green) and CBE (red) of the (a) N=24 and (b) N=36 $AlSi_N$-$CF_3$ NTs. Same coloring scheme as in Figure 1, with the additional F-atoms being colored purple.

**Table S8.** The calculated surface dipole density ($\mu_\sigma$), polarization (P), band gap (BG), vacuum aligned Valence Band (VBE) and Conduction Band (CBE) edges for the $AlSi_{24}$-$CF_3$ and $AlSi_{36}$-$CF_3$ NTs at PBE, PBE-D2 and VDWDF level.

| System | $\mu_\sigma$ [pC m$^{-1}$] | P [C m$^{-2}$] | BG [eV] | VBE [eV] | CBE [eV$^2$] |
|---|---|---|---|---|---|
| **N=24** | | | | | |
| PBE | 56.53 | 0.05862 | 4.104 | -5.351 | -1.247 |
| PBE-D2 | 56.50 | 0.05859 | 4.104 | -5.349 | -1.245 |
| VDWDF | 57.60 | 0.05900 | 3.964 | -5.768 | -1.803 |
| **N=36** | | | | | |
| PBE | 44.52 | 0.04683 | 4.252 | -5.501 | -1.249 |
| PBE-D2 | 44.53 | 0.04684 | 4.249 | -5.492 | -1.243 |
| VDWDF | 47.13 | 0.04837 | 4.062 | -5.811 | -1.749 |

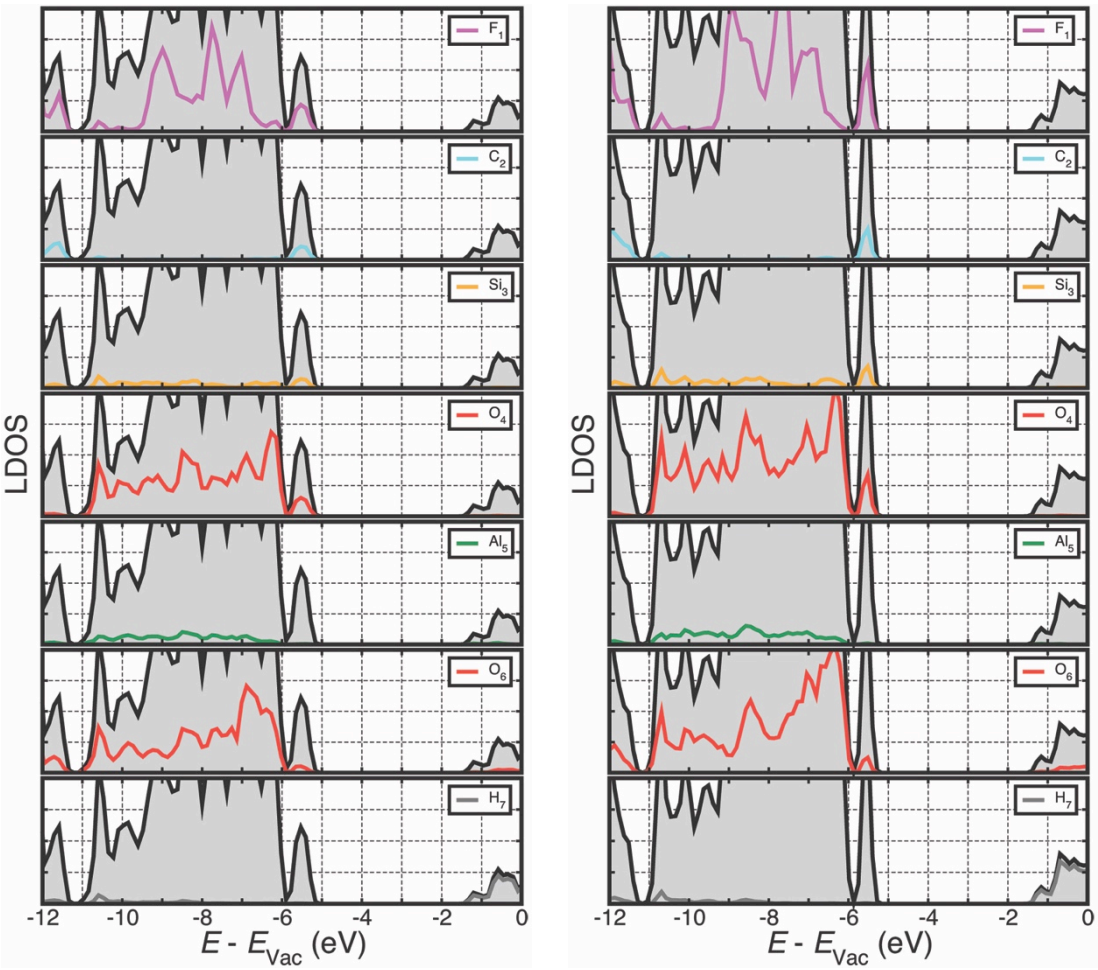



**Figure S18.** Vacuum-aligned **PBE** total DOS plot (filled grey) and layer resolved LDOS plots for the **$AlSi_{24}$-$CF_3$** (left) and **$AlSi_{36}$-$CF_3$** (right). See Figure 1a and S17 for the adopted layer-labeling.

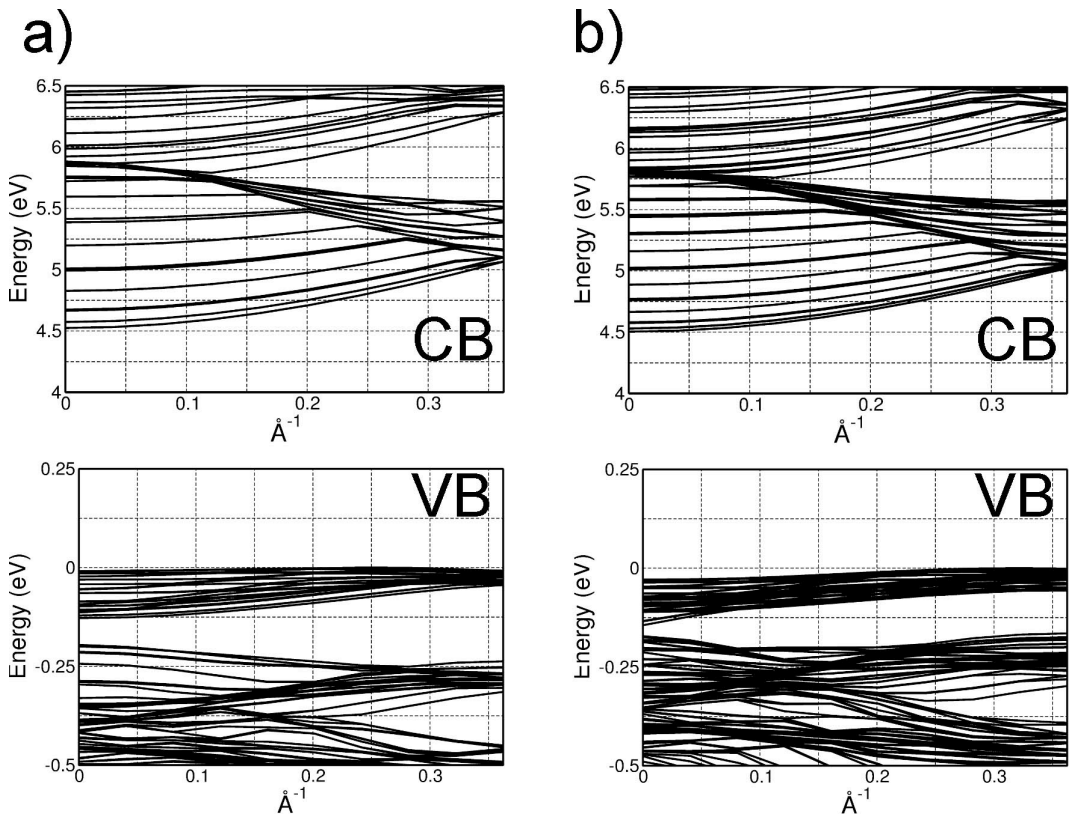



**Figure S19.** The calculated band structure along the NT-axis (ΓX direction, Ref. S7) for the methylated $AlSi_{24}$-Me (a) and $AlSi_{36}$-Me (b) NTs. VB: Valence Band, CB: Conduction Band. The energy scale has been referenced to the VB-maximum (0 eV). VB-maxima not at the centre of the Brilluoin zone (Γ-point) have previously been reported for other inorganic (ionic) nanotubes [S6].

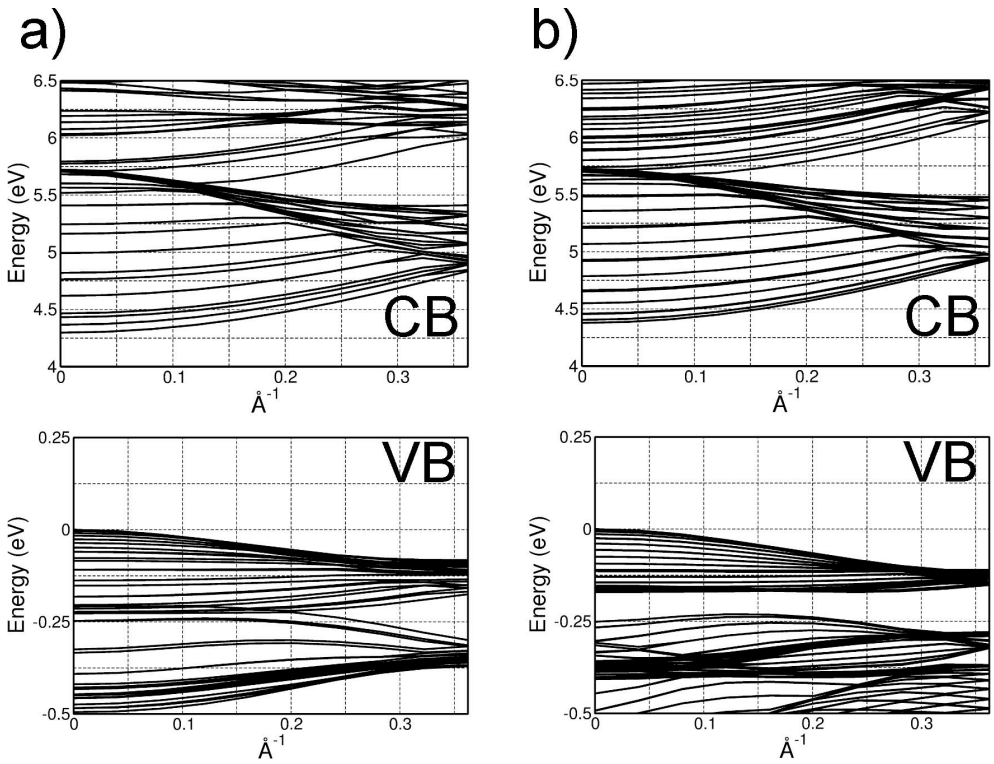



**Figure S20.** The calculated band structure along the NT-axis (ΓX direction, Ref. S7) for the pristine hydroxilated $AlSi_{24}$ (a) and $AlSi_{36}$ (b) NTs. VB: Valence Band, CB: Conduction Band. The energy scale has been referenced to the VB-maximum (0 eV). The computed results are in accordance with previously published PBE results for pristine (aluminosilicate) imogolite NTs [S7].

**Table S9** The calculated effective electron ($m_e$) and hole ($m_h$) masses, in units of rest electron mass ($m_0$), for $AlSi_{24}$-Me and $AlSi_{36}$-Me NTs and corresponding hydroxylated analogs ($AlSi_{24/36}$). Results for α-$Al_2O_3$, γ-$Al_2O_3$ (from Ref. [S8]) are reported for comparison.

| System | $m_e/m_0$ | $m_h/m_0$ |
|---|---|---|
| $AlSi_{24}$-Me | 0.81 | 7.41 |
| $AlSi_{36}$-Me | 0.79 | 5.77 |
| $AlSi_{24}$-Me | 0.80 | 1.86 |
| $AlSi_{36}$-Me | 0.77 | 1.74 |
| α-$Al_2O_3$ | 0.40 (Γ→A)<br>0.38 (⊥Γ→A) | 7.5 (⊥Γ→A)<br>0.35 (Γ→A) |
| γ-$Al_2O_3$ | 0.40 | 1.3 (Γ→K)<br>>>1 (⊥Γ→K) |

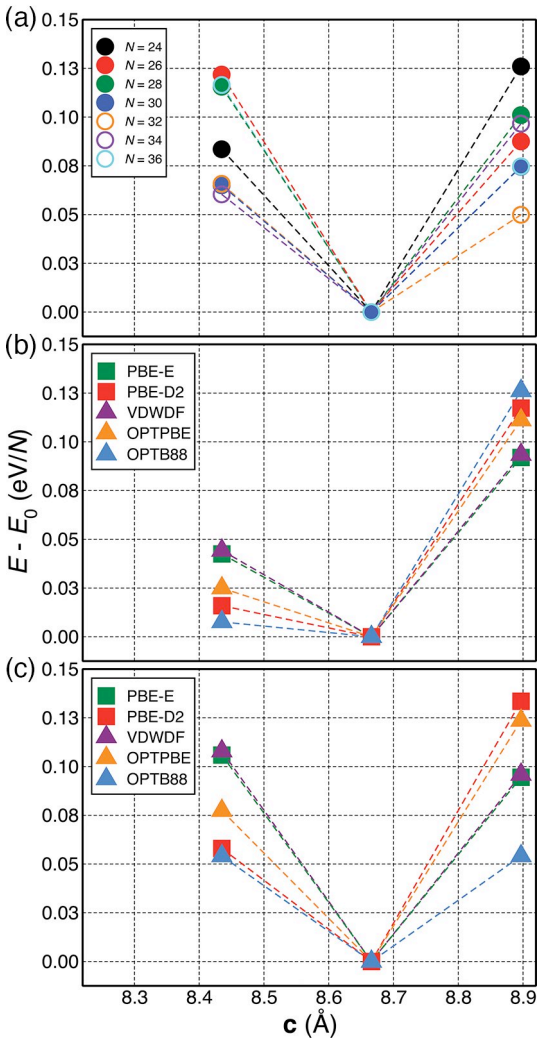



**Figure S21.** Relative DFT-energy, normalized to the number of Al-atoms in the NT (*N*) and referenced to the computed minimum, as a function of the NT-repeat unit length (*c*, see Fig. 1b) for the considered range of *N* and XC-functionals. *c* has been changed in multiple of the coarse FFT-grid separation [21] (0.231 Å) using the plane-wave optimized value from Ref. [11b] (c=8.666 Å) as starting point. a) the PBE energy minimum is computed for *c*=8.666 Å, regardless of *N* (i.e. of the NT radius). Regardless of the XC-functional used, *c*=8.666 Å is computed to yield an energy minimum also for the smallest $AlSi_{24}$-Me (b) and largest $AlSi_{36}$-Me (c) NTs, that bracket the whole range of considered *N*.

## 3. Supplementary References

[S1] J. D. Jackson, Classical Electrodynamics, John Wiley & Sons, Inc.

[S2] J. Junquera, M. H Cohen, K. M. Rabe, *J. Phys. Condens. Matt.* **19**, 213203 (2007).

[S3] C.-K. Skylaris, P. D. Haynes, A. A. Mostofi, M. C. Payne, *J. Chem. Phys.* **122** 084119 (2005).

[S4] G. Kresse, J. Furthmüller, *Phys. Rev. B* **54** 11169 (1996).

[S5] J.P. Perdew, K. Burke, M. Ernzerhof, *Phys. Rev. Lett.* **77** 3865 (1996).

[S6] J. Xiao, M. Long, X. Li., H. Xu, H. Huang, Y. Gao, *Sci. Rep.* **4**, 4327 (2014).

[S7] M. Zhao, Y. Xia, L. Mei, *J. Phys. Chem. C* **113**, 14834 (2009).

[S8] T. V Perevalov, A. V. Shaposhnikov, V. A. Gritsenko, Microelectron. Eng. **86**, 1915 (2009).